Rationalizing the Superior Catalytic Efficiency of Nickel Nitride vs Nickel Sulfide for Alkaline Hydrogen Evolution Reaction from Bubble Dynamics Study and Density Functional Theory (DFT) Calculations

Chinkit Tyagi, Pooja Basera, Corinne Lagrost, Valérie Bouquet, Franck Tessier, Marie-Caroline Jullien, Bruno Fabre

To cite this version:

Chinkit Tyagi, Pooja Basera, Corinne Lagrost, Valérie Bouquet, Franck Tessier, et al.. Rationalizing the Superior Catalytic Efficiency of Nickel Nitride vs Nickel Sulfide for Alkaline Hydrogen Evolution Reaction from Bubble Dynamics Study and Density Functional Theory (DFT) Calculations. ACS Catalysis, 2025, 15, pp.3823-3835. ⟨10.1021/acscatal.4c05777⟩. ⟨hal-04975408⟩

HAL Id: hal-04975408

https://hal.science/hal-04975408v1

Submitted on 31 Mar 2025

Rationalizing the Superior Catalytic Efficiency of Nickel Nitride vs. Nickel Sulfide for Alkaline Hydrogen Evolution Reaction From Bubble Dynamics Study and Density Functional Theory (DFT) Calculations

Chinkit Tyagi,[1] Pooja Basera[2,3], Corinne Lagrost,[1,4] Valérie Bouquet,[1] Franck Tessier,[1] Marie-Caroline Jullien,[5] and Bruno Fabre[1,]*

[1] CNRS, ISCR (Institut des Sciences Chimiques de Rennes) - UMR6226, Univ Rennes, Rennes F-35000, France

[2] Department of Chemical Engineering, Stanford University, Stanford, California 94305, United States

[3] SUNCAT Center for Interface Science and Catalysis, SLAC National Accelerator Laboratory, Menlo Park, California 94025, United States

[4] ScanMAT – UAR 2025, F-35000 Rennes, France

[5] CNRS, IPR (Institut de Physique de Rennes) - UMR 6251, Univ Rennes, Rennes F-35000, France.

ABSTRACT. Due to their high electronic conductivity, high catalytic activity and superior chemical stability, nickel nitrides and sulfides have been demonstrated to be cost-effective and robust electrocatalysts for achieving HER under alkaline conditions. Herein, we report on a simple and optimized approach to directly grow single-phase nickel nitride (Ni_3N) and nickel sulfide (Ni_3S_2) on a flat nickel substrate. Different preparation conditions are tested in order to achieve materials exhibiting the best electrocatalytic efficiency for HER. The optimized Ni_3N and Ni_3S_2 on nickel are obtained at 700°C for 30 min under ammonia gas flow and at 350°C for 1 h in 10 % H_2S/H_2 gas mixture, respectively. Ni_3N operate HER in 1M KOH more efficiently than Ni_3S_2, as supported by overpotential values of 0.189, 0.291 and 0.342 V measured at 10, 100 and 200 mA cm^{-2}, respectively, which are lower than those measured for Ni_3S_2, *i.e.* 0.204, 0.351 and 0.417 V. Remarkably, it is worth noticing that its HER activity competes with that of Pt for current densities higher than 200 mA cm^{-2}. Its superior catalytic activity is corroborated by additional cyclic voltammetry (Tafel slopes) and electrochemical impedance spectroscopy measurements. Moreover, Ni_3N and Ni_3S_2 are found to be stable over 45 h electrolysis at 10 mA cm^{-2} with a potential change of only 24 and 31 mV, respectively. To gain further understanding on the electrocatalytic HER activities of both materials, Density Functional Theory (DFT) calculations and *in situ* bubble dynamics study are performed. Owing to the more hydrophilic character of Ni_3N, smaller H_2 bubbles form and detach more rapidly from the surface which leads to a fast renewal of the active surface for HER. In contrast, for Ni_3S_2, both the bubble size and the retention time increase, leading to the adverse blockage of the active sites and requiring higher overpotential for HER.This observation perfectly aligns with DFT calculations, which show that H_2O adsorption is predominantly favored on the Ni_3N surface. Our work highlights that the use of a planar electrocatalyst support instead of foam-type porous one is essential to evaluate the alone contribution of the electrocatalyst on the electrogenerated gas bubble dynamics and consequently the impact on the catalytic performance.

KEYWORDS. Water Splitting, Hydrogen Evolution Reaction, Electrocatalysis, Bubble Dynamics, Nickel Nitrides, Nickel Sulfides

1. Introduction.

The production of dihydrogen (H_2) by electrolytic water splitting constitutes a carbon-free, clean and sustainable alternative to traditional steam reforming based on fossil fuels which is emitting greenhouse gases (CO_2 and CO) and is highly energy intensive.[1,2,3] In that context, alkaline water electrolysis has aroused a tremendous interest because it allows the use of cost-effective and Earth-abundant transition metals (e.g. Ni, Mo, Fe and Co) as efficient electrocatalysts for both hydrogen evolution reaction (HER) and oxygen evolution reaction (OER).[4,5,6] In particular, transition metal chalcogenides, phosphides, borides, nitrides, oxides and carbides have been intensively studied as electrocatalysts for these two half-reactions of interest, essentially owing to their high electronic conductivity, excellent catalytic activity and superior chemical stability.[7,8,9,10,11] Among these materials, nickel nitrides and sulfides have been demonstrated to be catalytically efficient for HER and other energy conversion reactions.[12,13,14,15,16,17] They can be prepared from the direct nitridation or sulfidation of nickel under NH_3 or H_2S-H_2 mixtures using various conditions (time, temperature, and gas mixture composition).[18,19,20] These electrocatalysts can be also produced in the form of nanostructures (nanosheets, nanorods and nanowires) using various methods, including hydrothermal, electrodeposition, chemical vapor deposition, and microwave-assisted methods.[21,22,23,24,25,26,27,28,29] Such a catalyst nanostructuring was found to be an effective strategy to enhance the electrocatalytic performance due to the high surface area and the facilitated release of the electrogenerated gas bubbles.[30] For the latter, it is worth recalling that gas bubbles evolving at the electrode surface may result in undesired blockage of active sites and negatively impact the performance of the electrocatalytic process.[31] This is a critical issue for industrial electrolyzers as bubble films formed at large scale (several hundred cm^2) electrodes can be more than 1 cm thick, leading to high Ohmic resistances and mass transfer barriers of the electrode reactions. As a result, a strong enhancement in the electrical power consumption of the electrolyzer may occur.[32] Such detrimental effects can be minimized by acting on the bubble dynamics, i.e. by facilitating and controlling the formation of small H_2 bubbles and shortening the retention time at the electrode surface before their release.[33,34] Besides the morphology of the electrocatalysts, their surface-wetting properties can also greatly influence the detachment of the gas bubbles and consequently the overall performance of the water splitting.[35,36,37,38,39]

Herein, we propose a simple and original approach to directly grow HER electrocatalysts, namely single-phase nickel nitride (Ni_3N) and nickel sulfide (Ni_3S_2), on a flat nickel substrate. These two catalysts were selected because (*i*) they exhibited different hydrophilic/aerophobic properties, and (*ii*) they showed the highest activities for alkaline HER among the other Ni nitride ($Ni_3N > Ni_4N$)[40,41,42,43,44] and sulfide ($Ni_3S_2 > NiS_2 > NiS$)[45,46,47] phases. Moreover, a flat Ni substrate was preferred to porous Ni one (e.g. Ni foam) in order to eliminate the effect of the porosity of the substrate on the dynamics of electrogenerated H_2 bubbles[48] for investigating only the intrinsic effects of the prepared catalyst. After optimization of the preparation conditions of these materials, the best performing electrodes were further characterized using multiple surface characterization techniques to get more insights on their morphological, topographical, and wetting properties. Finally, the *in-situ* bubble formation was monitored by videography to understand the effects of surface hydrophilicity or aerophobicity on the electrochemical HER activity of the catalytic electrodes in 1 M KOH solution. Complementary Density Functional Theory (DFT) calculations provided essential information on the thermodynamics of alkaline HER at both materials.

2. Materials and Methods

2.1. Chemicals. Nickel foil (NF) with a thickness of 0.5 mm, 20% platinum (Pt) on graphitized carbon, poly(vinylidene fluoride) (PVDF) binder, and *N*-methyl-2-pyrrolidone (NMP) were purchased from Sigma-Aldrich. VULCAN carbon black and KOH were bought from Cabot and Thermo Fisher Scientific, USA, respectively. All chemicals were used as received, and ultra-pure water (Veolia Water-STI) with a resistivity of 18.2 MΩ cm was used to prepare the aqueous solutions.

2.2. Direct growth of Ni_3N (Ni_3N@NF) and Ni_3S_2 (Ni_3S_2@NF) on NF. Before the thermal treatment, the NF piece (1 x 1.5 cm^2) was successively cleaned under sonication for 10 min in acetone, absolute ethanol, and ultrapure water to remove impurities and was dried using an argon flow gun. Cleaned NF was thermally treated at various temperatures and times in a tubular furnace with a heating rate of ~10 °C/min under ammonia (NH_3, $\geq$ 99.96 %) and H_2S/H_2 (10%/90 %) gas flow to generate Ni_3N (Ni_3N@NF) and Ni_3S_2 (Ni_3S_2@NF), respectively, on NF. The Ni_3N@NF electrodes were obtained at 700 °C for 30 min, 1 h or 2 h under ammonia gas flow. To prepare Ni_3S_2@NF, cleaned NF was heated at different temperatures (300, 350, 400, 450, and 500 °C) for 30 min under H_2S/H_2 gas mixture to grow the nickel sulfide phase on NF. Ni_3S_2@NF electrodes were further optimized for the sulfidation time (from 30 min to 4 h) at an optimized temperature of 350 °C.

2.3. Instrumentation. X-ray diffraction (XRD) patterns of synthesized materials on NF were obtained using Bruker D8 Advance diffractometer (Cu Kα1 radiation, λ = 1.5406 Å) with a LynxEye fast detector.

JSM-7100F JEOL Scanning electron microscope (SEM) equipped with an X-Max 50 mm^2 EDS detector (Oxford Instruments) was used for images and elemental mapping.

The profilometry measurements were conducted at three different areas (500 μm x 500 μm) for each electrode using a Bruker Dektak X profilometer having a Stylus B-type tip with a curvature radius of 12.5 µm, and average roughness was calculated after tilt angle correction.

An automated Krüss Easy Drop goniometer was used for contact angle measurements using a 1M KOH solution. Contact angles were determined using the Tangent 2 fitting model with 2.0 μL droplets of 1M KOH at three different spots for each electrode.

XPS data have been collected by a NEXSA G2 (ThermoFischer Scientific) spectrometer using the Al Kα X-ray source working at 1486.6 eV with a spot size of 200 μm². Survey spectra (0-1000 eV) were acquired with an analyzer pass energy of 200 eV (1 eV/step); high-resolution spectra used pass energy of 50 eV (0.1 eV/step). Binding energies were referenced to C 1s peak at 284.8 eV (adventitious carbon). The core level spectra were peak-fitted using the CasaXPS Software, Ltd. Version 2.3.25PR1.0. U2 Tougaard or Shirley background subtraction was used for the spectral analysis. The peak areas were normalized by the manufacturer-supplied sensitivity factor (S_{C1s} = 1, , S_{O1s} = 2.88, S_{Ni2p} = 20.76, S_{N1s} = 1.68 and S_{S2p} = 1.88). For each sample, XPS survey spectra were recorded at three different locations, and we did not observe any difference.

The electrochemical measurements were performed at room temperature in a three-electrode configuration on a BioLogic SP-200 single-channel electrochemical workstation equipped with an AC frequency response analyzer (FRA). An alkaline solution (1.0 M KOH, pH = 14 ± 0.1) was used as the electrolytic solution. Bare or modified NF was masked from one side with Teflon tape and used as the working electrode (1 cm^2 geometric surface area). A graphite rod and Hg/HgO (filled with 1.0 M KOH) were used as the counter and reference electrodes, respectively. A 20 nm-thick Pt film-coated NF electrode was used for comparison. It was obtained by magnetron sputtering of a Pt target on NF. All HER polarization curves were recorded by linear sweep voltammetry (LSV) at 5 mV s^{-1} with 95% *iR* compensation using the automated *iR*-correction function of the potentiostat. The current densities (j) were normalized by the geometric surface area (1 cm^2) of NF electrodes, and overpotential vs. log (current density) (η vs. log j) linear curves were plotted to determine the corresponding Tafel slopes. All potentials measured vs. Hg/HgO were converted versus the reversible hydrogen electrode (RHE) according to the equation given below:

$$E_{\mathrm{RHE}} = E_{\mathrm{Hg/HgO}} + 0.059\ \mathrm{pH} + E^{0}_{\mathrm{Hg/HgO}} \text{ with } E^{0}_{\mathrm{Hg/HgO}} = +0.102\ \mathrm{V} \quad (1)$$

where $E_{\mathrm{Hg/HgO}}$ is applied potential versus the used reference electrode.

Electrochemical impedance spectroscopy (EIS) measurements were recorded at an applied overpotential of 0.2 V over a frequency range from 100 kHz to 100 mHz (50 frequencies, logarithmic distribution) at 10 mV amplitude. The double-layer capacitance (C_{dl}) was calculated using cyclic voltammograms (CVs) recorded in the non-Faradaic region at various scan rates (20 to 100 mV s^{-1}). C_{dl} (in mF cm^{-2}) corresponds to the slope value of the $\Delta j/2$ vs. v plots where Δj is the difference between the anodic and cathodic current densities and v is the potential scan rate. Electrochemically active surface area (ECSA) was calculated from C_{dl} and the specific capacitance (C_{s}) of a flat metallic Ni surface that was assumed to be 20 μF cm^{-2} (ECSA = $C_{\mathrm{dl}}/C_{\mathrm{s}}$).[49] The long-term stability tests of the prepared electrodes were examined using chronopotentiometry at an applied current density of -10 mA cm^{-2}.

Prior to electrochemical measurements, Ni_3S_2 was activated by successively cycling the Ni_3S_2@NF electrode at 20 mV/s between 0.1 and -0.57 V vs RHE in 1 M KOH solution (50 scans). As previously reported, such a procedure led to an increase in the surface area of the electrode and in the number of exposed active sites.[50,51,52]

For studying bubble dynamics, H_2 bubbles were produced in a three-electrode cell system with vertical configuration under the same conditions (1.0 M KOH, pH = 14 ± 0.1) at the current density of -5 and -10 mA cm^{-2} without any convection. The bubble dynamics was monitored using a Fastcam UX50 (Photron) through a stereomicroscope (Leica MZ FLIII) placed aside of the cell. The bubbles were mapped manually using ImageJ freeware, and the average bubble density and size distribution were estimated for all the electrodes during HER.

2.4. Computational details. DFT calculations were performed as implemented in the Vienna *Ab Initio* Simulation package. Projector-augmented wave (PAW) pseudopotentials were employed to describe the ion−electron interactions.[53] The Perdew-Burke-Ernzerhof (PBE) exchange-correlational functional was used for optimizing the atomic position of the structures.[54,55] The DFT optimized bulk structures of Ni, Ni_3N and Ni_3S_2 were used to construct the initial slabs, with a 2 x 2 in-plane supercell employed for slab construction. During the relaxation of the surface layers, only atomic positions were allowed to relax. A five-layer thick slab was started, with the top two layers relaxed while the internal layers were kept frozen to mimic the bulk. The surfaces were optimized using a 4 × 4 × 1 Monkhorst-Pack grid,[56] and a kinetic energy cutoff was set to 500 eV. Structural relaxation was performed until the forces were smaller than 0.02 eV/Å. For single-point energy calculations, the PBE functional was used with the energy convergence tolerance set to 0.01 meV. The Gibbs free energies (ΔG) of each step along the reaction pathway at T = 298 K were estimated using the equation (2):

$$[\Delta G = \Delta E - T\Delta S + \Delta EZPE] \tag{2}$$

where ΔE, ΔS, and $\Delta EZPE$ are the changes in enthalpy (obtained from DFT total energy), entropy, and zero-point energy, respectively. Zero-point energies for the adsorbed and the free molecules were computed using DFT calculations, while the entropic contributions for free molecules were obtained from the thermodynamic tables.[57] For the adsorption of water molecules on surfaces, charge transfer was computed by examining electronic accumulation or depletion upon molecular adsorption by comparing the charge densities in the combined system and individual components. This analysis yielded the expression for charge transfer between the slab and the adsorbate (or vice versa), represented by the equation (3):

$$\Delta\rho = \rho_{\text{slab + adsorb}} - (\rho_{\text{slab}} + \rho_{\text{adsorb}}) \tag{3}$$

where $\rho_{\text{slab + adsorb}}$, ρ_{slab}, and ρ_{adsorb} denote the total electronic charge density of the entire system containing the Ni, Ni_3N and Ni_3S_2 slab and the adsorbate, the electronic charge density of the slab, and the electronic charge density of the adsorbate (H_2O), respectively.

3. Results and Discussion.

3.1. Preparation/Optimization and Characterization of Ni_3N@NF and Ni_3S_2@NF. Different temperatures and durations for nitridation or sulfidation of NF have been tested and their effects on HER electrocatalytic properties of the resulting materials have been examined. The Ni_3N phase was directly grown on NF (Ni_3N@NF) from the thermal treatment of cleaned NF at 700°C for 30 min, 1 h or 2 h under ammonia (≥ 99.96%) gas flow. For the preparation of Ni_3S_2, cleaned NF was heated at different temperatures (300, 350, 400, 450, and 500°C) for 30 min under H_2S/H_2 (10 %/90 %) gas mixture to grow the nickel sulfide phase on NF. To further optimize the

Ni_3S_2 composition, the effect of the sulfidation time (from 30 min to 4 h) at an optimized temperature of 350°C was also examined.

The X-ray diffraction (XRD) patterns and the respective HER activity of thermally treated NF at 700°C for 30 min, 1 h, and 2 h under NH_3 are shown in Figures S1. All three diffraction patterns exhibited characteristic peaks indexed to hexagonal nickel nitride (Ni_3N) phase (JCPDS card no. 01-089-5144 or 00-010-0280) and cubic nickel (Ni) (JCPDS card no. 00-004-0850) coming from NF substrate. It was found that the nitridation duration had only a limited impact on the HER activity of the resulting materials.

The diffraction patterns and HER activity of NF thermally treated at 300, 350, 400, 450, and 500°C for 30 min in a 10 % H_2S/H_2 atmosphere are shown in Figure S2. At the temperature of 350°C, the XRD pattern confirmed the growth of the Ni_3S_2 phase as the main phase (JCPDS card no. 00-044-1418 or 00-030-0863). Furthermore, the material prepared at 350°C and 400°C for 30 min showed the highest HER activity among all the sulfidation temperatures (Figure S2b). Additionally, the XRD patterns and HER activity of materials prepared at an optimized temperature of 350°C using different sulfidation times are shown in Figure S3. NF treated at 350°C for 1 h showed characteristic peaks attributed to the desired Ni_3S_2 phase (JCPDS card no. 00-044-1418) along with a further improvement of HER activity. To sum up, best HER performing Ni_3N and Ni_3S_2 on NF were obtained at 700°C for 30 min under ammonia gas flow and at 350°C for 1 h in 10 % H_2S/H_2 gas mixture, respectively. Their corresponding XRD patterns along with that of bare NF (BNF) are shown in Figure 1. These Ni_3N@NF and Ni_3S_2@NF electrodes were selected for further characterizations and their alkaline HER activity was examined in more details (*vide supra*).

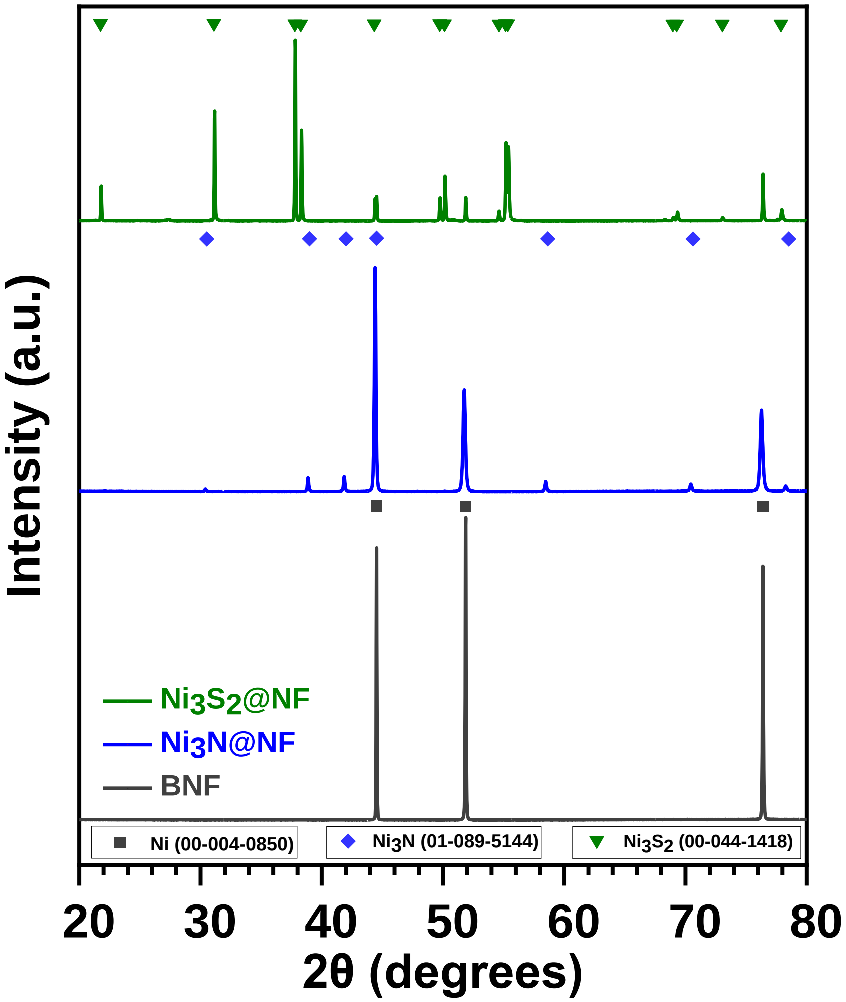

Figure 1. XRD diffraction patterns of bare nickel foil (BNF) and NF thermally treated at 700°C for 30 min under NH_3 (Ni_3N@NF), and at 350°C for 1 h under H_2S (Ni_3S_2@NF).

Ni_3N@NF and Ni_3S_2@NF materials were further characterized by scanning electron microscopy (SEM), profilometry, and contact angle measurements to get more insights into the morphological, topographical, and wetting properties, respectively. As shown in Figures 2 and S4, the SEM images of Ni_3N@NF and Ni_3S_2@NF showed a rough and porous structure uniformly covering Ni. Consistent with that, the average root-mean-square roughness measured by profilometry was 176 ± 6, 732 ± 19, and 902 ± 55 nm for BNF, Ni_3N@NF, and Ni_3S_2@NF, respectively. Globally, the morphological characteristics of both materials were relatively comparable. Additionally, water contact angles measured with 1 M KOH showed that the hydrophilic character of the materials increased in the following order: BNF (97 ± 5°) < Ni_3S_2@NF (70 ± 2°) < Ni_3N@NF (40 ± 1°) (Figures 2 and S5). Furthermore, the elemental mapping and the energy dispersive X-ray spectroscopy (EDS) analysis of these electrodes evidenced the homogeneous distribution of the expected elements, namely, Ni, N, and S (Figures S6 and S7) with a very small quantity of detected oxygen.

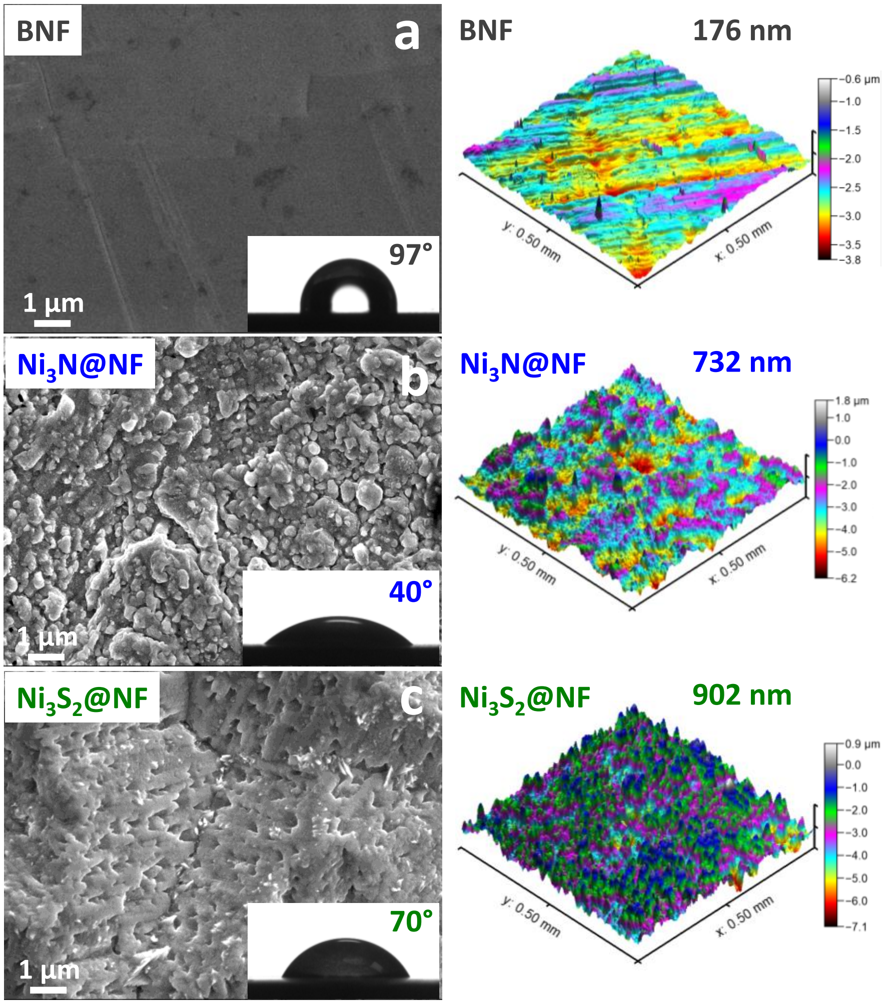

Figure 2. SEM images, contact angle, and profilometry measurements of (a) bare nickel foil (BNF), (b) Ni_3N@NF and (c) Ni_3S_2@NF.

In order to complete the XRD analyses, X-ray photoelectron spectroscopy (XPS) was also employed to probe in more details the chemical composition at the outermost surface of the materials (5-10 nm depth). It is worth noting that XPS measurements also investigate amorphous parts of the materials in contrast to XRD. Comparison of the survey spectrum of BNF with those of optimized Ni_3N@NF and Ni_3S_2@NF revealed as expected the presence of new photoelectrons peaks for the elemental species N or S, respectively (Figure S8). Core level spectra in the Ni 2p, N 1s and S 2p regions were subsequently recorded for Ni_3N@NF and Ni_3S_2@NF to probe the chemical states of the corresponding species. The Ni 2p spectra displayed the 2p doublet structure with an energy separation of 17.5 eV (Figure 3). Peak-fitting of the Ni $2p_{3/2}$ signals for the three samples led to two main lines and a minor contribution with their corresponding satellite peaks (dashed and dotted lines in Fig. 3) that could be attributed to Ni-Ni bonding, $Ni(OH)_2$ and NiO species, respectively.[22,58,59,60,61,62] The presence of NiO and $Ni(OH)_2$ species also supported by the peak-fitting of the O 1s photoelectron signal (Figure S9) indicates that the materials' surface was partially oxidized. The Ni_3N@NF and Ni_3S_2@NF materials presented nearly the same spectra than that of metal BNF. However, the peak due to Ni-Ni bond (in BNF) was shifted to higher binding energy values by 0.5 eV for Ni_3N@NF and Ni_3S_2@NF due to the formation of Ni-N and Ni-S bonds (Table S1).[62,63] For Ni_3N@NF, the nitridation of the nickel materials was further assessed by the decomposition of the signal of the N 1s photoelectron peak (Figure 3c). The major component at 397.7 eV is in agreement with Ni-N bonding.[59,64] Signals due to oxidized nitrogen species were also observed as minor contributions. Such observations were consistent with either the partial oxidation of the surface or the presence of residual species due to the incomplete transformation of ammonia. Regarding Ni_3S_2@NF, the S 2p spectrum brought a very interesting piece of information. The decomposition of the signal was quite complex with several pairs of doublets due to the spin orbit splitting at the 2p level with a peak-to-peak separation of 1.2 eV between both S $2p_{3/2}$ and S $2p_{1/2}$ components. As expected, all these doublets exhibit intensity ratio of 2:1. On the higher binding energy side, S $2p_{3/2}$ peaks at 168.4 and 166.3 eV were related to sulfur oxidized species that contributed in a minor portion. Elemental sulfur, probably due to the incomplete transformation of H_2S, could also be detected at 164 eV at low content. A main doublet was observed at 161.2 and 162.3 eV. A second doublet at 162.5 and 163.7 eV also contributed to the signal but in lesser extent. This latter doublet could be assigned to Ni_3S_2 while the signal at 161.2 eV corresponded to NiS if one refers to XPS data reported for millerite (NiS) and heazlewoodite (Ni_3S_2) compounds.[65,66] This observation indicates that the outermost surface of optimized Ni_3S_2@NF mainly consisted of NiS. NiS could be the initial product during the sulfidation reaction and could transfer to the nickel surface in a non-stoichiometric Ni_3S_2 zone as an amorphous phase being not detected by XRD. Alternatively, the NiS amorphous phase could be produced upon exposure to ambient air.

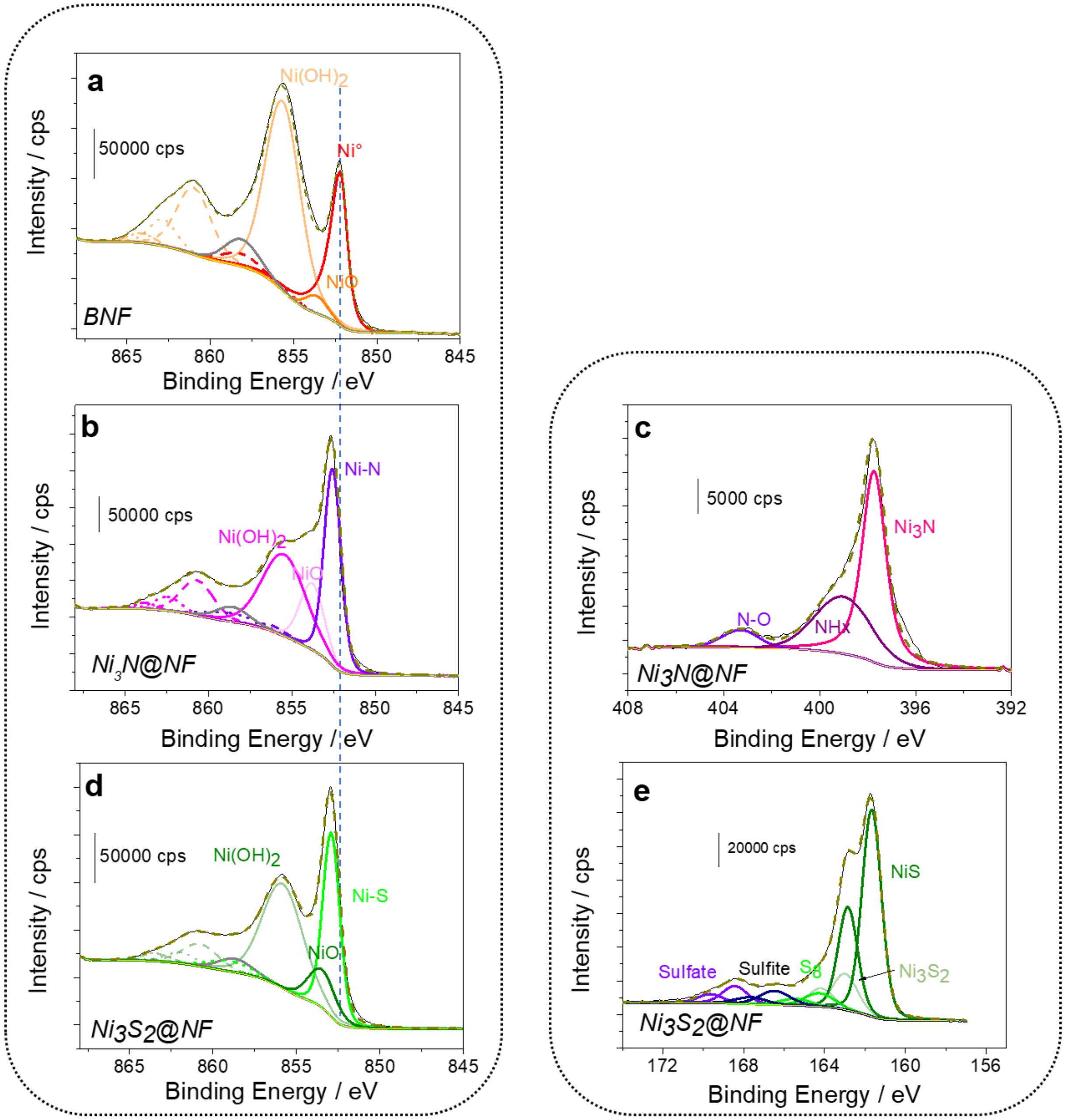

Figure 3. Peak-fitted high-resolution core-level spectra of Ni 2p$_{3/2}$ region (left panel) for BNF (a), Ni$_3$N@NF (b) and Ni$_3$S$_2$@NF (d), of N 1s and S 2p regions (right panel) for Ni$_3$N@NF (c) and Ni$_3$S$_2$@NF (e), respectively. Experimental data are the black solid lines, fittings are represented by colored solid (main peaks) and dashed/dotted (satellites) lines, respectively. The resulting fitting envelopes are the dark yellow dashed lines. For Ni 2p, the gray component at 858.4 ± 0.4 eV corresponds to interband losses.

3.2. Electrocatalytic Activity for Alkaline HER. The electrocatalytic HER activity of the optimized Ni_3N@NF and Ni_3S_2@NF was evaluated in an alkaline aqueous solution (1.0 M KOH, pH 14) along with the reference BNF electrode. As shown in Figure 4a, Ni_3N@NF exhibited the highest HER activity, as supported by the lowest onset potential of -0.075 V vs RHE (set arbitrarily at 1 mA cm^{-2}) and the lowest *iR*-corrected overpotential values of 0.189 (η_{10}), 0.291 (η_{100}) and 0.342 V (η_{200}) measured at 10, 100 and 200 mA cm^{-2}, respectively (Table 1). These values are 125, 65, and 24 mV higher than those determined for benchmark 20 nm-thick Pt film-coated NF (20nm Pt@NF). Remarkably, it is worth noticing that its HER activity competes with that of Pt for current densities higher than 200 mA cm^{-2}. In comparison, Ni_3S_2@NF yielded overpotentials $\eta_{10} = 0.204$ V, $\eta_{100} = 0.351$ V and $\eta_{200} = 0.417$ V which were expectedly lower than those measured for BNF, i.e. 0.292, 0.422 and 0.503 V, respectively (Table 1).

The superior activity of Ni_3N@NF for HER was also confirmed by its Tafel slope of 92 mV dec^{-1} which was smaller than those of Ni_3S_2@NF (98 mV dec^{-1}) and BNF (124 mV dec^{-1}) (Fig. 4b). Such Tafel slopes are significantly higher compared to the value obtained for the Pt@NF electrode (59 mV dec^{-1}). These findings suggest that the HER on Ni-based materials is controlled by the Volmer reaction step, which involves the electrochemical adsorption of hydrogen atoms onto the catalyst's active sites. In contrast, for Pt, the Tafel reaction, which is the combination of two adsorbed hydrogen atoms to form molecular hydrogen (H_2), appears to be the rate-determining step.[67]

To gain further insights on the electron-transfer kinetics, EIS measurements were performed for all electrodes at an applied overpotential of 0.2 V and in the frequency range 10^5 to 10^{-1} Hz.

The data are presented in the form of Nyquist diagrams, i.e. by plotting the imaginary part (Z'') vs the real part (Z') of the complex impedance ($Z = Z' + iZ''$) as a function of frequency f. All Nyquist plots are characterized by a semicircle and can be adequately fitted by assuming the simplified Randles equivalent electrical circuit comprising a resistance (the cell resistance R_s) in series with the charge-transfer resistance (R_{ct}) and a constant phase element (CPE) in parallel (Figure 4c). For this circuit model, the semicircle's diameter on the Z' axis corresponds to R_{ct}. Consistent with previous electrochemical data, the R_{ct} of Ni_3N@NF (7.8 Ω) was found to be smaller than that calculated for Ni_3S_2@NF (9.7 Ω) and BNF (49.3 Ω), confirming faster charge-transfer kinetics for HER.

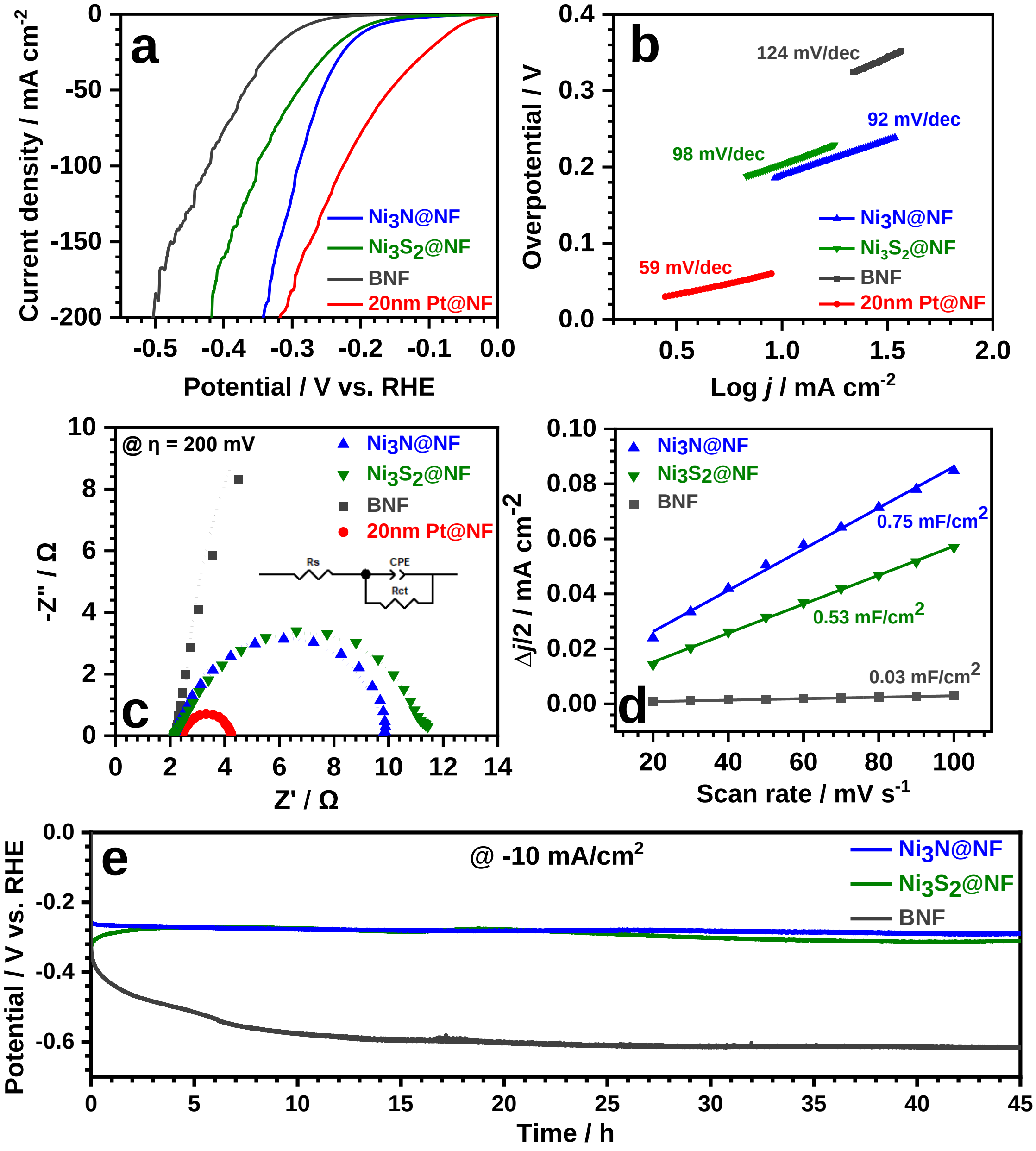

Figure 4. a) *iR*-corrected HER polarization curves in 1 M KOH solution at 5 mV/s of BNF, Ni_3N@NF and Ni_3S_2@NF compared with benchmark Pt@NF, b) corresponding Tafel slopes, c) EIS Nyquist plots and fitted curves using the simplified Randles circuit (inset) at an applied overpotential of 0.2 V, d) $\Delta j/2$ vs v plots where Δj is the difference between the anodic and cathodic charging current densities (extracted from cyclic voltammograms shown in Figure S10)

used for determining C_{dl} for the different electrodes and e) chronopotentiometric curves at an applied current density of -10 mA cm^{-2}.

Electrode	Onset potential / V vs RHE [a]	η_{10} / V [b]	η_{100}, η_{200} / V [b]	Tafel slope / mV dec^{-1}	R_{ct} / Ω [c]	C_{dl} / mF cm^{-2}	ECSA / cm^2
BNF	-0.212	0.292	0.422, 0.503	124	49.3	0.03	1.5
Ni_3N@NF	-0.075	0.189	0.291, 0.342	92	7.8	0.75	37.5
Ni_3S_2@NF	-0.109	0.204	0.351, 0.417	98	9.7	0.53	26.5
Pt@NF	-0.005	0.064	0.226, 0.318	59	1.9	n.a.	n.a.

Table 1. HER Electrocatalytic Parameters for Different Modified NF Cathodes in 1 M KOH.

[a] Set arbitrarily at 1 mA cm^{-2}. [b] *iR*-corrected overpotential at a current density of 10, 100 and 200 mA cm^{-2}. [c] Determined from Nyquist plots at 200 mV overpotential.

Moreover, because the considered electrodes showed a certain roughness, the estimation of the electrochemically active surface area (ECSA) for each electrode is strongly recommended to account for differences in the density of electrocatalytically active sites. ECSA can be commonly determined using ECSA = $C_{\mathrm{dl}}/C_{\mathrm{s}}$ where C_{dl} is the double-layer capacitance extracted from cyclic voltammograms recorded in a non-Faradaic potential window at different scan rates (Figure S10) and C_{s} is the specific capacitance of flat Ni (see the Materials and Methods section for details).[49] Consistent with aforementioned electrochemical data, Ni_3N@NF exhibited C_{dl} and ECSA values slightly larger than those determined for Ni_3S_2@NF, namely 0.75 mF cm^{-2} and 37.5 cm^2 against 0.53 mF cm^{-2} and 26.5 cm^2 (Fig. 4d), highlighting a higher density of active sites. This demonstrates that the superior density of active sites in Ni_3N@NF contributes to the enhanced HER activity. Furthermore, we have checked that the ECSA value calculated for BNF ($1.5 \ cm^2$) was close to $1 \ cm^2$, as expected for a perfectly flat surface.

In addition to the electrocatalytic activity, the long-term stability of BNF, Ni_3N@NF, and Ni_3S_2@NF electrodes was also examined in 1 M KOH solution at an applied current density of -10 mA cm^{-2}. The corresponding chronopotentiometric curves revealed that Ni_3N@NF and Ni_3S_2@NF were stable over 45 h electrolysis with a potential change of only 24 and 31 mV, respectively (Fig. 4e). In comparison, a much higher potential shift of 153 mV was measured for BNF electrode.

After the HER stability test, the high-resolution core level spectra for the Ni 2p, N 1s and S 2p regions (Figure S13), as well as the EDS-estimated atomic ratios of the characteristic elements (Figures S11 and S12), were consistent with a decrease in the amounts of N and S for both electrodes concomitantly with an increase in the content of O. Such a result can be ascribed to the surface hydroxylation phenomenon during the stability test which was probably caused by chemical interactions of the electrocatalytic surface with hydroxide ions (OH^-) present in the strongly alkaline electrolyte.

3.3. DFT Calculations. The electrocatalytic HER activities were better understood by performing DFT calculations to explore the thermodynamics of HER in an alkaline environment (Figure 5a). In contrast to the acidic HER mechanism, the rate-determining step in alkaline HER is likely the barrier related to water dissociation steps (Volmer).[68] The Ni(111), Ni_3N(111), and Ni_3S_2(110) facets were modeled based on the XRD results (Fig. 1). The Gibbs free energy change toward HER for these surfaces was then calculated using these models. For Ni(111), a high energy barrier of 1.01 eV for the water dissociation step was observed, mainly attributed to the weak adsorption of OH* on Ni sites. Similarly, the water dissociation energy for Ni_3S_2 was found to be as high as 0.70 eV due to the weak bonding strength between Ni and adsorbed OH (OH*). The adsorption energy of H (H*) on the S site at Ni_3S_2 was calculated to be -0.19 eV. On the other hand, for Ni_3N, the stronger adsorption of OH* at Ni sites and H* at N sites significantly reduces the energy barrier for water dissociation to 0.49 eV. These findings align with You *et al.*, where nitrogen acts as a promoter on an N-doped Ni(111) surface, facilitating hydrogen extraction from adsorbed water.[69] Herein, the DFT calculations show that the Ni_3N (111) surface exhibits the lowest water activation energy and near-zero energy for hydrogen evolution, making it highly favorable for alkaline HER, consistent with the experimental results. Next, the optimized surfaces with H_2O adsorbed on Ni sites are presented in Figure 5b. It was found that H_2O preferentially adsorbs to the Ni top site on all surfaces via the O atom. The adsorption energy, distance between H_2O and the surface metal atom (Ni-O), O-H bond length, bond angles of water, and Bader charges of the Ni active site before and after H_2O adsorption are listed in Table 2. The Ni-O bond lengths between the O atom and the surface metal atom Ni are 2.18 Å, 2.06 Å, and 2.15 Å for the Ni, Ni_3N, and Ni_3S_2 surfaces, respectively. The shorter Ni-O bond length observed for the Ni_3N surface results in a more negative adsorption energy compared to the Ni_3S_2 and Ni surfaces (Fig. 5c). This reduction in bond length, along with O-H distances measured at 0.98 Å and a bond angle of 106°, indicates a weakening of O-H bonds, which contributes to an enhanced HER. The charge density difference analysis, also shown in the insets of Figure 5c, reveals charge depletion (cyan color) at the Ni surface and charge accumulation (yellow) at the O atom, which is more prominent for the Ni_3N surface. The Bader charge analysis supports these findings, showing an enhancement of charge at the Ni active site after water adsorption (Table 2). Figure 5d presents the density of states (DOS) for the Ni, Ni_3N, and Ni_3S_2

surfaces. The projected DOS of Ni_3N and Ni_3S_2 reveals that the energy bands surrounding the Fermi level are composed of Ni 3d, N 2p, and S 2p orbitals. While Ni has low DOS at the Fermi level, Ni_3N and Ni_3S_2 exhibit a metallic state with a high density of occupied electrons around the Fermi level. These occupied electrons are transferred to H_2O upon adsorption on the surface, leading to charge depletion at the interface, and enhanced adsorption energy.

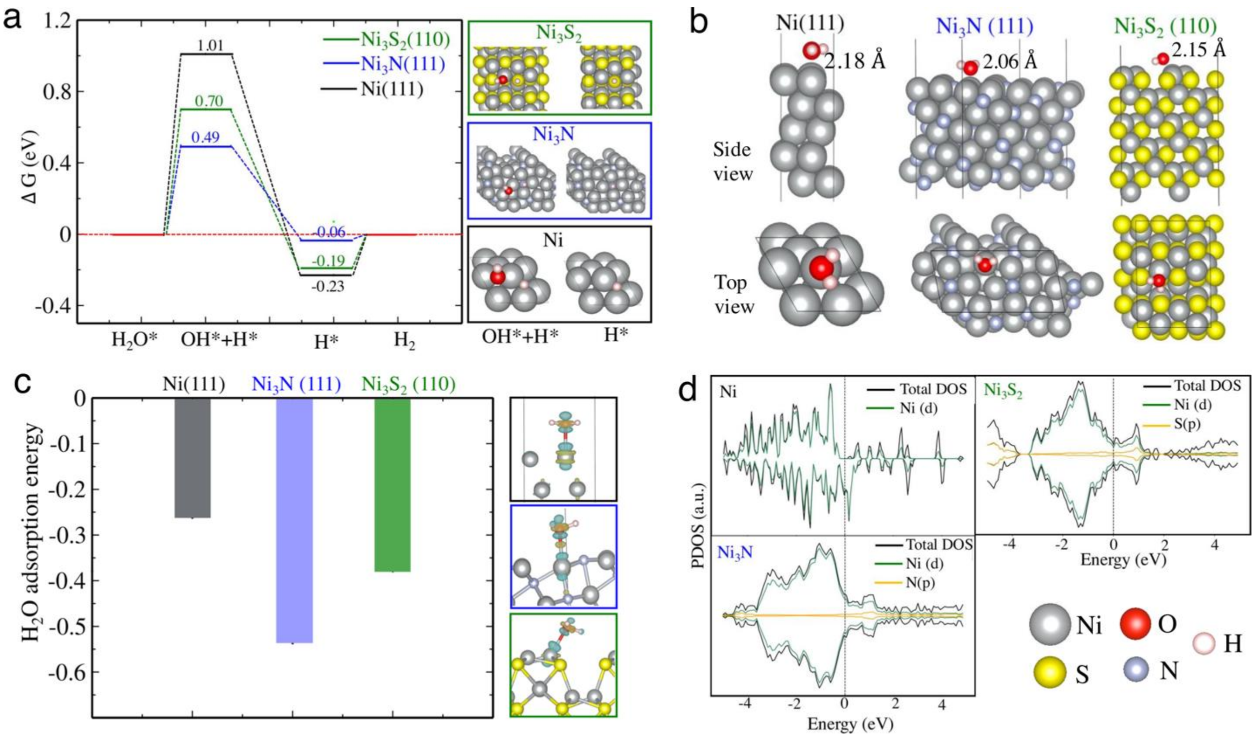

Figure 5. a) Gibbs free energy diagrams for alkaline HER pathway on Ni(111), $Ni_3N(111)$, and $Ni_3S_2(110)$ surfaces. The right panel shows the modeled transition state (OH* + H*) and the H* adsorbed state. b) Optimized side and top views of Ni(111), $Ni_3N(111)$, and $Ni_3S_2(110)$ with H_2O. c) H_2O adsorption energy and charge density differences (cyan: depletion, yellow: accumulation) with an iso-surface value of 0.05 e/Å^3. d) Total and partial density of states for Ni(111), $Ni_3N(111)$, and $Ni_3S_2(110)$ surfaces.

Table 2. Calculated adsorption energies (E_{ads}), Ni-O distances, O-H bond lengths, and bond angles in water. Bader charges of the Ni active site [q(Ni)] are computed for both the pristine and H_2O-adsorbed surface.

Surface	E_{ads} (eV)	d(Ni-O) (Å)	d(O-H) (Å)	H-O-H (°)	q(Ni) (e^-)	
					Pristine	H_2O_{ads}
Ni(111)	-0.26	2.18	0.983	104.9	-0.03	0.12
Ni_3N(111)	-0.54	2.06	0.981, 0.980	106.1	0.19	0.34
Ni_3S_2(110)	-0.38	2.15	0.982, 0.977	104.9	0.40	0.48

3.4. Bubble Dynamics at the Electrocatalytic Cathodes. The visualization of H_2 bubbles electrogenerated at the catalytic electrodes was monitored by videography using a high-speed camera (Figure S14). Therefore, photographs have been captured from videos recorded during the electrolysis of cathodes in 1 M KOH in order to determine the average bubble density and size distribution. A current density of -10 mA cm^{-2} was selected to monitor the formation of H_2 bubbles at the electrode surface. Figure 6 displays snapshots of the H_2 bubbles produced on the different substrates (additional photographs and movie are shown in Figures S15-S17 and Movie S1). Table 3 summarizes the physico-chemical properties and the quantitative data extracted from these snapshots, i.e. bubble diameter and bubble density. At first glance, the bubble diameter decreased upon decreasing contact angle and Ni_3N@NF thus produced the smallest bubbles. This can be well understood if we consider that the more hydrophilic the substrate, the more the liquid tends to spread and consequently the less bubbles stay attached. A deeper study on the bubble statistics is given on Figure 7 which displays the bubble diameter histograms for the three substrates. It is clear that the bubble diameter distribution is well centered around a mean value for Ni_3N@NF, i.e. the bubble radius is well controlled, while the distributions are almost equi-distributed for the two other electrodes. The properties of the interface, hydrophilic *vs.* hydrophobic, have here a direct impact on the control of the size of the bubbles produced, but also on their residence time on the electrodes. In fact, the distribution centred around a mean value of 50-60 μm for Ni_3N@NF indicates a much shorter residence time than for the other two electrodes for which the distributions are spread out, indicating an uncontrolled residence time on the electrodes.

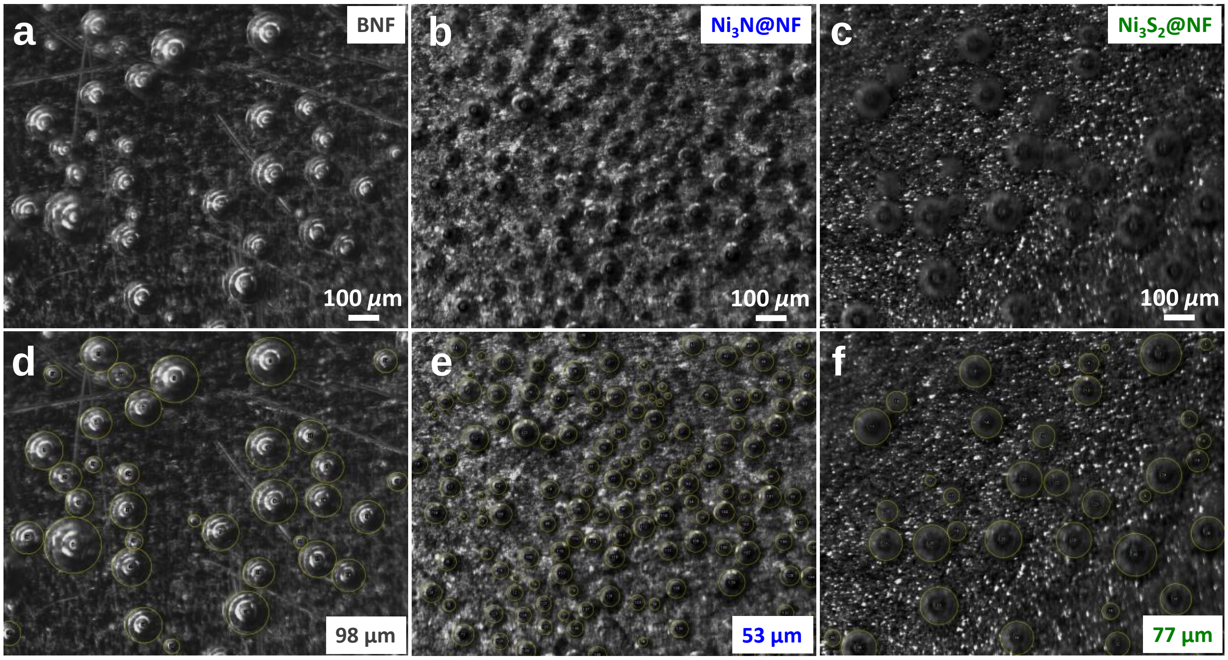

Figure 6. Photographs of H_2 bubbles (highlighted by yellow circles) evolved at BNF (a, d), Ni_3N@NF (b, e) and Ni_3S_2@NF (c, f) electrodes at -10 mA cm^{-2} in 1M KOH. Numbers in the white boxes (d-f) correspond to the average size of the bubbles.

Table 3. Evolved H_2 Bubble Size and Density for Different Modified NF Cathodes in 1 M KOH.

Electrode	Contact angle / °	Roughness / nm	Bubble diameter / μm	Bubble density / per mm^2
BNF	97 ± 5	176 ± 6	98 ± 35	25 ± 3
Ni_3N@NF	40 ± 1	732 ± 19	53 ± 15	99 ± 9
Ni_3S_2@NF	70 ± 2	902 ± 55	77 ± 34	24 ± 4

More surprising was the bubble density for the three substrates. Despite the Ni_3N@NF was more hydrophilic, it showed the highest bubble density with a factor of 4 compared to the two other substrates. Actually, if we measure the contact area of the bubble, i.e. the wetting area A_W for a single bubble, it is given by:

$$A_W = \pi R_W^2 = \pi[R\sin(\theta)]^2 \tag{4}$$

with R_w the wetting radius (Figure S18). This successively gives in our range of parameters for the mean radii: $A_{W,Ni_3N@NF} = 3650\ \mu m^2$, $A_{W,Ni_3S_2@NF} = 16500\ \mu m^2$ and $A_{W,BNF} = 29700\ \mu m^2$. A single H_2 bubble on Ni_3N@NF occupied 4 to 5 times less area of the electrode than on Ni_3S_2@NF, and 8 times less area than on the BNF substrate. This leads to the following total wetted areas: $A_{Ni_3N@NF} = 0.36\ mm^2$, $A_{Ni_3S_2@NF} = 0.39\ mm^2$ and $A_{BNF} = 0.74\ mm^2$. The more hydrophilic substrate is the less covered by H_2 bubbles and thus screens less the electrodes.

Finally, a higher hydrophilicity leads to smaller bubbles, larger bubble densities and less H_2 wetted areas.

Furthermore, both the H_2 bubble size and retention time increased upon increasing the hydrophobic character of the catalytic material, which led to the blockage of active sites and increased the dead surface area. This resulted in low HER activity and current fluctuations as observed on the LSV curves of Ni_3S_2@NF and BNF at current densities higher than 100 mA cm^{-2} (Figure 4a). Note that this retention time can be reinforced by triple line pinning that depends on the roughness of the substrate, leading to coupled effects that are out of the scope of the present paper. Due to the more hydrophilic nature of Ni_3N@NF, smaller H_2 bubbles formed and detached more rapidly from the surface which provided large surface area for ongoing hydrogen production. This observation perfectly aligns with DFT calculations, which show that H_2O adsorption is predominantly favored on the Ni_3N surface (Fig. 5c). As a result, this electrode achieved HER with lower overpotential and superior catalytic efficiency.

In a nutshell, based on our observations, it can be concluded that the release of H_2 bubbles is more efficient for the most hydrophilic substrate, Ni_3N@NF, than for the other electrodes (Figures S15-S17 and Table 3).

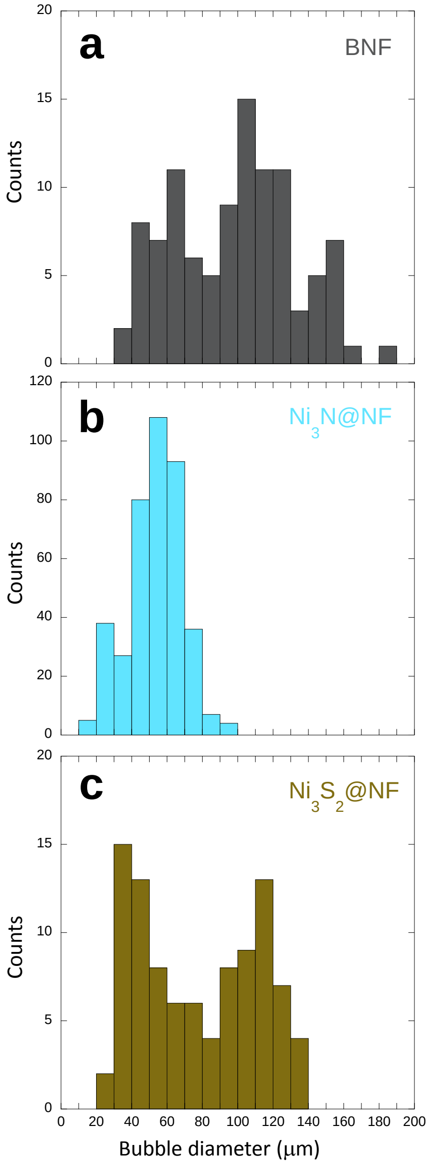

Figure 7. Size distribution of H_2 bubbles electrogenerated on BNF (a), Ni_3N@NF (b) and Ni_3S_2@NF (c) electrodes.

4. Conclusion

To sum up, nickel nitride (Ni_3N) and nickel sulfide (Ni_3S_2) were conveniently grown in one step on nickel foil (NF) through the thermal treatment of cleaned NF under NH_3 and 10% H_2S/H_2, respectively. The hydrophilic character of these materials in 1 M KOH solution was found to increase in the following order: NF < Ni_3S_2@NF < Ni_3N@NF, which is corroborated by DFT results. The most hydrophilic electrode Ni_3N@NF showed the best HER activity, in terms of onset potential and overpotential at 10, 100 and 200 mA cm^{-2}. Complementary *in situ* bubble dynamics study has enabled us to understand the impact of surface hydrophilicity on the electrochemical HER activity in 1 M KOH solution. Owing to its hydrophilic and probably aerophobic character, Ni_3N@NF produced a high density of about 50 μm-diameter H_2 bubbles which were rapidly released from the electrode surface, leading to a fast renewal of the active surface for HER. Such an efficient release of H_2 bubbles from Ni_3N@NF can explain why its HER activity competes with that of Pt for current densities higher than 200 mA cm^{-2}. In contrast, for BNF and rougher Ni_3S_2@NF, both the bubble size and the retention time increased, leading to the adverse blockage of the active sites and requiring higher overpotential for HER. Our findings highlight that the impact of material roughness on both the bubble size and density is therefore somewhat weak.

This work constitutes a first step toward advanced and high-performance catalytic electrodes. In that context, combining the electrocatalyst nanostructuring with a porous or textured electrode substrate represents an effective strategy to significantly enhance the HER performance of our systems thanks to a further enhanced release of H_2 bubbles. Finally, it would be also valuable to investigate the effects of both the electrolyte countercation and concentration on the *in-situ* bubble dynamics since it has been demonstrated by Koper and co-workers that such experimental factors may significantly affect bubble coalescence and detachment due to the solutal Marangoni effect.[70,71]

ASSOCIATED CONTENT

Supporting Information. Additional XRD patterns, SEM images, EDS and XPS spectra, electrochemical data, angle contact measurements, photographs of the evolved H_2 bubbles and movie on the H_2 bubble release at -5 and -10 mA cm^{-2}. The Supporting Information is available free of charge on the ACS Publications website.

AUTHOR INFORMATION

Corresponding Author

* **Bruno Fabre —** CNRS, ISCR (Institut des Sciences Chimiques de Rennes)-UMR6226, Univ Rennes, Rennes F-35000, France. E-mail: bruno.fabre@univ-rennes1.fr

Author Contributions

B. F. and C. T. conceived the project, designed the experiments, analyzed the data, and wrote the manuscript. V. B. and F. T. contributed in the synthesis of Ni_3S_2@NF and Ni_3N@NF, respectively. F. T. performed and analyzed the XRD data. C. L. performed and analyzed the XPS data. M.-C. J. provided the experimental environment for the bubbles dynamics and contributed to the data analysis. P. B. carried out the DFT theoretical calculations and analyzed the data. All authors contributed to the discussion of the results. All authors participated in editing the paper and have given approval to the final version of the manuscript.

Funding Sources

This project has received financial support from the CNRS through the 80|Prime program.

ACKNOWLEDGMENT

Bruno Fabre, Marie-Caroline Jullien and Chinkit Tyagi acknowledge the Centre National de la Recherche Scientifique (CNRS) for the research funding and Ph.D. research grant (80|Prime program). The XRD and XPS measurements have been performed on OSIRIX, THEMIS, and ASPHERYX platforms, respectively (ScanMAT, UAR 2025 University of Rennes-CNRS; CPER-FEDER 2015-2020). The authors are grateful to Stéphanie Lamy and Sophie Ollivier for their assistance in the cutting of NF and preparation of Ni_3S_2@NF, respectively. Loic Joanny and Francis Gouttefangeas are fully acknowledged for SEM images and EDS analyses performed at CMEBA (ScanMAT, University of Rennes). Laurent Courbin, Thomas Mabit and Florian Scholkopf (IPR, UMR 6251, Univ Rennes, France) are thanked for their help in bubble dynamics study. Pooja Basera thanks Dr. Viswanath Pasumarthi from Purdue University for helpful discussions.

Table of Contents (TOC)

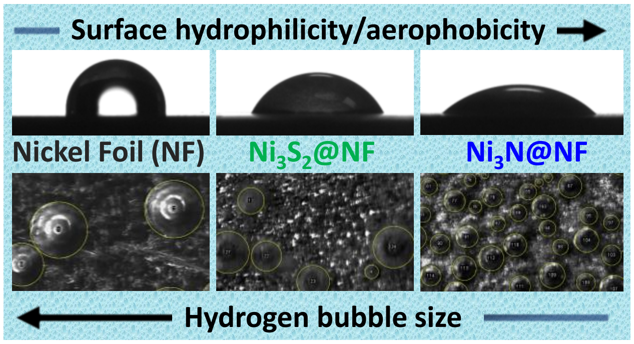

REFERENCES

---

(1) Terlouw, T.; Bauer, C.; McKenna, R.; Mazzotti, M. Large-Scale Hydrogen Production via Water Electrolysis: A Techno-Economic and Environmental Assessment. *Energy Environ. Sci.* **2022**, *15*, 3583–3602.

(2) Kumar, S. S.; Lim, H. An overview of water electrolysis technologies for green hydrogen production. *Energy Rep.* **2022**, *8*, 13793-13813.

(3) International Energy Agency. The Future of Hydrogen, 2019.

(4) Ledendecker, M.; Mondschein, J. S.; Kasian, O.; Geiger, S.; Göhl, D.; Schalenbach, M.; Zeradjanin, A.; Cherevko, S.; Schaak, R. E.; Mayrhofer, K. Stability and Activity of Non-Noble-Metal-Based Catalysts Toward the Hydrogen Evolution Reaction. *Angew. Chemie Int. Ed.* **2017**, *56*, 9767–9771.

(5) Wu, H.; Feng, C.; Zhang, L.; Zhang, J.; Wilkinson, D. P. Non-Noble Metal Electrocatalysts for the Hydrogen Evolution Reaction in Water Electrolysis. *Electrochem. Energ. Rev*. **2021**, *4*, 473–507.

(6) Zou, X.; Zhang, Y. Noble Metal-Free Hydrogen Evolution Catalysts for Water Splitting. *Chem. Soc. Rev.* **2015**, *44*, 5148–5180.

(7) Anantharaj, S.; Ede, S. R.; Sakthikumar, K.; Karthick, K.; Mishra, S.; Kundu, S. Recent Trends and Perspectives in Electrochemical Water Splitting with an Emphasis on Sulfide, Selenide, and Phosphide Catalysts of Fe, Co, and Ni: A Review. *ACS Catal.* **2016**, *6*, 8069–8097.

(8) Zhong, Y.; Xia, X.; Shi, F.; Zhan, J.; Tu, J.; Fan, H. J. Transition Metal Carbides and Nitrides in Energy Storage and Conversion. *Adv. Sci.* **2016**, *3*, 1500286.

---

(9) Benck, J. D.; Hellstern, T. R.; Kibsgaard, J.; Chakthranont, P.; Jaramillo, T. F. Catalyzing the Hydrogen Evolution Reaction (HER) with Molybdenum Sulfide Nanomaterials. *ACS Catal*. **2014**, *4*, 3957–3971.

(10) Kawashima, K.; Márquez, R. A.; Smith, L. A.; Vaidyula, R. R.; Carrasco-Jaim, O. A.; Wang, Z.; Son, Y. J.; Cao, C. L.; Mullins, C. B. A Review of Transition Metal Boride, Carbide, Pnictide, and Chalcogenide Water Oxidation Electrocatalysts. *Chem. Rev.* **2023**, *123*, 12795-13208.

(11) Yu, M.; Budiyanto, E.; Tüysüz, H. Principles of Water Electrolysis and Recent Progress in Cobalt-, Nickel-, and Iron-Based Oxides for the Oxygen Evolution Reaction. *Angew. Chem. Int. Ed.* **2022**, *61*, e202103824.

(12) Wang, H.; Li, J.; Li, K.; Lin, Y.; Chen, J.; Gao, L.; Nicolosi, V.; Xiao, X.; Lee, J.-M. Transition Metal Nitrides for Electrochemical Energy Applications. *Chem. Soc. Rev.* **2021**, *50*, 1354-1390.

(13) Chandrasekaran, S.; Yao, L.; Deng, L.; Bowen, C.; Zhang, Y.; Chen, S.; Lin, Z.; Peng, F.; Zhang, P. Recent Advances in Metal Sulfides: from Controlled Fabrication to Electrocatalytic, Photocatalytic and Photoelectrochemical Water Splitting and Beyond. *Chem. Soc. Rev.* **2019**, *48*, 4178-4280.

(14) Huo, L.; Jin, C.; Jiang, K.; Bao, Q.; Hu, Z.; Chu, J. Applications of Nickel-Based Electrocatalysts for Hydrogen Evolution Reaction. *Adv. Energy and Sustainability Res.* **2022**, *3*, 2100189.

(15) Shalom, M.; Ressnig, D.; Yang, X.; Clavel, G.; Fellinger, T. P.; Antonietti, M. Nickel Nitride as an Efficient Electrocatalyst for Water Splitting. *J. Mater. Chem. A* **2015**, *3*, 8171–8177.

---

(16) Tareen, A. K.; Priyanga, G. S.; Khan, K.; Pervaiz, E.; Thomas, T.; Yang, M. Nickel-Based Transition Metal Nitride Electrocatalysts for the Oxygen Evolution Reaction. *ChemSusChem* **2019**, *12*, 3941–3954.

(17) Zhao, Y.; Jin, B.; Vasileff, A.; Jiao, Y.; Qiao, S. Z. Interfacial Nickel Nitride/Sulfide as a Bifunctional Electrode for Highly Efficient Overall Water/Seawater Electrolysis. *J. Mater. Chem. A* **2019**, *7*, 8117–8121.

(18) Stoklosa, A.; Stringer, J. Studies of the Kinetics of Nickel Sulfidation in H_2S-H_2 Mixtures in the Temperature Range 450-600°C. *Oxid. Met.* **1977**, *11*, 263-276.

(19) Leineweber, A.; Lienert, F.; Shang, S. L.; Liu, Z.-K.; Mittemeijer, E. J. Ni_3N Compound Layers Produced by Gaseous Nitriding of Nickel Substrates; Layer Growth, Macrostresses and Intrinsic Elastic Anisotropy. *J. Mater. Res.* **2012**, *27*, 1531–1541.

(20) Fonovic, M.; Leineweber, A.; Mittemeijer, E. J. Nitrogen Uptake by Nickel in NH_3–H_2 Atmospheres. *Surf. Eng.* **2014**, *30*, 16-20.

(21) Liang, J.; Zhang, B.; Shen, H.; Yin, Y.; Liu, L.; Ma, Y.; Wang, X.; Xiao, C.; Kong, J.; Ding, S. Self-Supported Nickel Nitride Nanosheets as Highly Efficient Electrocatalysts for Hydrogen Evolution. *Appl. Surf. Sci.* **2020**, *503*, 144143.

(22) Gao, D.; Zhang, J.; Wang, T.; Xiao, W.; Tao, K.; Xue, D.; Ding, J. Metallic Ni_3N Nanosheets with Exposed Active Surface Sites for Efficient Hydrogen Evolution. *J. Mater. Chem. A* **2016**, *4*, 17363–17369.

(23) Balogun, M. S.; Zeng, Y.; Qiu, W.; Luo, Y.; Onasanya, A.; Olaniyi, T. K.; Tong, Y. Three-Dimensional Nickel Nitride (Ni_3N) Nanosheets: Free Standing and Flexible Electrodes for Lithium Ion Batteries and Supercapacitors. *J. Mater. Chem. A* **2016**, *4*, 9844–9849.

---

(24) Li, G.; Wu, X.; Guo, H.; Guo, Y.; Chen, H.; Wu, Y.; Zheng, J.; Li, X. Plasma Transforming $Ni(OH)_2$ Nanosheets into Porous Nickel Nitride Sheets for Alkaline Hydrogen Evolution. *ACS Appl. Mater. Interfaces* **2020**, *12*, 5951–5957.

(25) Wang, H.; Xiong, J.; Cheng, X.; Fritz, M.; Ispas, A.; Bund, A.; Chen, G.; Wang, D.; Schaaf, P. Ni_3N-Coated Ni Nanorod Arrays for Hydrogen and Oxygen Evolution in Electrochemical Water Splitting. *ACS Appl. Nano Mater.* **2020**, *3*, 10986–10995.

(26) Zhang, D.; Li, J.; Luo, J.; Xu, P.; Wei, L.; Zhou, D.; Xu, W.; Yuan, D. Ni_3S_2 Nanowires Grown on Nickel Foam as an Efficient Bifunctional Electrocatalyst for Water Splitting with Greatly Practical Prospects. *Nanotechnology* **2018**, *29*, 245402.

(27) Chen, M.; Su, Q.; Kitiphatpiboon, N.; Zhang, J.; Feng, C.; Li, S.; Zhao, Q.; Abudula, A.; Ma, Y.; Guan, G. Heterojunction Engineering of Ni_3S_2/NiS Nanowire for Electrochemical Hydrogen Evolution. *Fuel* **2023**, *331*, 125794.

(28) Chen, J.; Chen, J.; Ling, Y.; Lu, Z.; Zhang, Z. Efficient Hydrogen Evolution Reaction on Ni_3S_2 Nanorods with a P/N Bipolar Electrode Prepared by Dealloying Sulfurization of NiW Amorphous Alloys. *ACS Appl. Energy Mater.* **2020**, *3*, 5745–5755.

(29) Liao, Y.; Pan, K.; Pan, Q.; Wang, G.; Zhou, W.; Fu, H. In Situ Synthesis of a NiS/Ni_3S_2 Nanorod Composite Array on Ni Foil as a FTO-Free Counter Electrode for Dye-Sensitized Solar Cells. *Nanoscale* **2015**, *7*, 1623–1626.

(30) Li, M.; Xie, P.; Yu, L.; Luo, L.; Sun, X. Bubble Engineering on Micro-/Nanostructured Electrodes for Water Splitting. *ACS Nano* **2023**, *17*, 23299-23316.

(31) Angulo, A.; van der Linde, P.; Gardeniers, H.; Modestino, M.; Fernández Rivas, D. Influence of Bubbles on the Energy Conversion Efficiency of Electrochemical Reactors. *Joule* **2020**, *4*, 555–579.

(32) Zeng, K.; Zhang, D. Recent Progress in Alkaline Water Electrolysis for Hydrogen Production and Applications. *Prog. Energy Combust. Sci.* **2010**, *36*, 307-326.

(33) German, S. R.; Edwards, M. A.; Ren, H.; White, H. S. Critical Nuclei Size, Rate, and Activation Energy of H_2 Gas Nucleation. *J. Am. Chem. Soc.* **2018**, *140*, 4047−4053.

(34) German, S. R.; Edwards, M. A.; Chen, Q.; Liu, Y.; Luo, L.; White, H. S. Electrochemistry of Single Nanobubbles. Estimating the Critical Size of Bubble-Forming Nuclei for Gas-Evolving Electrode Reactions. *Faraday Discuss.* **2016**, *193*, 223−240.

(35) Cheng, X.; Du, Z.-D.; Ding, Y.; Li, F.-Y.; Hua, Z.-S.; Liu, H. Bubble Management for Electrolytic Water Splitting by Surface Engineering: A Review. *Langmuir* **2023**, *39*, 16994-17008.

(36) Xu, W.; Lu, Z.; Sun, X.; Jiang, L.; Duan, X. Superwetting Electrodes for Gas-Involving Electrocatalysis. *Acc. Chem. Res.* **2018**, *51*, 1590-1598.

(37) Andaveh, R.; Darband, G. B.; Maleki, M.; Rouhaghdam, A. S. Superaerophobic/Superhydrophilic Surfaces as Advanced Electrocatalysts for the Hydrogen Evolution Reaction: A Comprehensive Review. *J. Mater. Chem. A* **2022**, *10*, 5147–5173.

(38) Kim, B. K.; Kim, M. J.; Kim, J. J. Impact of Surface Hydrophilicity on Electrochemical Water Splitting. *ACS Appl. Mater. Interfaces* **2021**, *13*, 11940–11947.

(39) Liu, G.; Wong, W. S. Y.; Kraft, M.; Ager, J. W.; Vollmer, D.; Xu, R. Wetting-Regulated Gas-Involving (Photo)Electrocatalysis: Biomimetics in Energy Conversion. *Chem. Soc. Rev.* **2021**, *50*, 10674–10699.

(40) Li, J.; Yao, C.; Kong, X.; Li, Z.; Jiang, M.; Zhang, F.; Lei, X. Boosting Hydrogen Production by Electrooxidation of Urea over 3D Hierarchical Ni_4N/Cu_3N Nanotube Arrays. *ACS Sustainable Chem. Eng.* **2019**, *7*, 13278-13285.

---

(41) Li, J.; Zhu, Z.; Huang, Y.; Wang, F.; Balogun, M.-S. Ni_3N: A Multifunctional Material for Energy Storage and Electrocatalysis. *Materials Today Energy* **2022**, *26*, 101001.

(42) Hu, S.; Feng, C.; Wang, S.; Liu, J.; Wu, H.; Zhang, L.; Zhang, J. Ni_3N/NF as Bifunctional Catalysts for Both Hydrogen Generation and Urea Decomposition. *ACS Appl. Mater. Interfaces* **2019**, *11*, 13168−13175.

(43) Liu, W.; Xia, T.; Ye, Y.; Wang, H.; Fang, Z.; Du, Z.; Hou, X. Self-Supported Ni_3N Nanoarray as an Efficient Nonnoble-Metal Catalyst for Alkaline Hydrogen Evolution Reaction. *Int. J. Hydrogen Energy* **2021**, *46*, 27037−27043.

(44) Song, F.; Li, W.; Yang, J.; Han, G.; Liao, P.; Sun, Y. Interfacing Nickel Nitride and Nickel Boosts both Electrocatalytic Hydrogen Evolution and Oxidation Reactions. *Nat Commun* **2018**, *9*, 4531.

(45) Jiang, N.; Tang, Q.; Sheng, M.; You, B.; Jiang, D. E.; Sun, Y. Nickel Sulfides for Electrocatalytic Hydrogen Evolution under Alkaline Conditions: A Case Study of Crystalline NiS, NiS_2, and Ni_3S_2 Nanoparticles. *Catal. Sci. Technol.* **2016**, *6*, 1077–1084.

(46) Li, Y. T.; Bu, Y. F.; Chen, X. Y.; Zhu, T. L.; Wang, J.; Kawi, S.; Zhong, Q. Facile Dynamic Synthesis of Homodispersed Ni_3S_2 Nanosheets as a High-Efficient Bifunctional Electrocatalyst for Water Splitting. *ChemCatChem* **2019**, *11*, 1320−1327.

(47) Ren, H. N.; Huang, Z. H.; Yang, Z. Y.; Tang, S. J.; Kang, F. Y.; Lv, R. T. Facile Synthesis of Free-Standing Nickel Chalcogenide Electrodes for Overall Water Splitting. *J. Energy Chem*. **2017**, *26*, 1217−1222.

(48) Kou, T.; Wang, S.; Shi, R.; Zhang, T.; Chiovoloni, S.; Lu, J. Q.; Chen, W.; Worsley, M. A.; Wood, B. C.; Baker, S. E. et al. Periodic Porous 3D Electrodes Mitigate Gas Bubble Traffic

during Alkaline Water Electrolysis at High Current Densities. *Adv. Energy Mater.* **2020**, *10*, 2002955.

(49) Lasia, A.; Rami, A. Kinetics of Hydrogen Evolution on Nickel Electrodes. *J. Electroanal. Chem. Interfacial Electrochem*. **1990**, *294*, 123−141.

(50) Jiang, N.; Bogoev, L.; Popova, M.; Gul, S.; Yano, J.; Sun, Y. Electrodeposited Nickel-Sulfide Films as Competent Hydrogen Evolution Catalysts in Neutral Water. *J. Mater. Chem. A* **2014**, *2*, 19407–19414.

(51) Shang, X.; Chi, J.-Q.; Wang, Z.-B.; Dong, B.; Zhao, J.-C.; Li, X.-H.; Yan, K.-L.; Wang, L.; Chai, Y.-M.; Liu, C.-G. Microwave Annealing Promoted In-Situ Electrochemical Activation of Ni_3S_2 Nanowires for Water Electrolysis. *J. Cat.* **2018**, *368*, 112-119.

(52) Yanga, C.; Gaoa, M. Y.; Zhang, Q. B.; Zeng, J. R.; Li, X. T.; Abbott, A. P. In-Situ Activation of Self-Supported 3D Hierarchically Porous Ni_3S_2 Films Grown on Nanoporous Copper as Excellent pH-Universal Electrocatalysts for Hydrogen Evolution Reaction. *Nano Energy* **2017**, *36*, 85-94.

(53) Kresse, G.; Joubert, D. From Ultrasoft Pseudopotentials to the Projector Augmented-Wave Method. *Phys. Rev. B* **1999**, *59*, 1758-1774.

(54) Perdew, J. P.; Wang, Y. Accurate and Simple Analytic Representation of the Electron-Gas Correlation Energy. *Phys. Rev. B* **1992**, *45*, 13244-13249.

(55) Blöchl, P. E. Projector Augmented-Wave Method. *Phys. Rev. B.* **1994**, *50*, 17953–17979.

(56) Monkhorst, H. J.; Pack, J. D. Special Points for Brillouin-Zone Integrations. *Phys. Rev. B* **1976**, *13*, 5188-5192.

(57) Hinnemann, B.; Moses, P. G.; Bonde, J.; Jorgensen, K. P.; Nielsen, J. H.; Horch, S.; Chorkendorff, I.; Norskov, J. K. Biomimetic Hydrogen Evolution: MoS_2 Nanoparticles as Catalyst for Hydrogen Evolution. *J. Am. Chem. Soc.* **2005**, *127*, 5308−5309.

(58) Yuan, Y.; Zhou, Y.; Shen, H.; Rasaki, S. A.; Thomas, T.; Wang, J.; Wang, C.; Wang, J.; Yang, M. Holey Sheets of Interconnected Carbon-Coated Nickel Nitride Nanoparticles as Highly Active and Durable Oxygen Evolution Electrocatalysts. *ACS Appl. Energy Mater.* **2018**, *1*, 6774-6780.

(59) Singh, S.; Verma, R.; Kaul, N.; Sa, J.; Punjal, A.; Prabhu, S.; Polshettiwar, V. Surface Plasmon-Enhanced Photo-Driven CO_2 Hydrogenation by Hydroxy-Terminated Nickel Nitride Nanosheets. *Nature Commun.* **2023**, *14*, 2551.

(60) Peng, Y.; He, H. Novel Heterostructure Cu_2S/Ni_3S_2 Coral-Like Nanoarrays on Ni Foam to Enhance Hydrogen Evolution Reaction in Alkaline Media. *RSC Adv.* **2021**, *11*, 39493-39502.

(61) Kwak, M.; Bok, J.; Lee, B.-H.; Kim, J.; Seo, Y.; Kim, S.; Choi, H.; Ko, W.; Antink, W. H.; Lee, C. W.; Yim, G. H.; Seung, H.; Park, C.; Lee, K.-S.; Kim, D.-H.; Hyeon, T.; Yoo, D. Ni Single Atoms on Carbon Nitride for Visible-Light-Promoted Full Heterogeneous Dual Catalysis. *Chem. Sci.* **2022**, *13*, 8536-8542.

(62) Kang, J. S.; Park, M.-A.; Kim, J.-Y.; Park, S. H.; Chung, D. Y.; Yu, S.-H.; Kim, J.; Park, J.; Choi, J.-W.; Lee, K. J.; Jeong, J.; Ko, M. J.; Ahn, K.-S.; Sung, Y.-E. Reactively Sputtered Nickel Nitride as Electrocatalytic Counter Electrode for Dye- and Quantum Dot-Sensitized Solar Cells. *Sci. Rep.* **2015**, *5*, 10450.

(63) Liu, C.; Shi, X.-R.; Yue, K.; Wang, P.; Zhan, K.; Wang, X.; Xia, B. Y.; Yan, Y. S-Species-Evoked High-Valence $Ni^{2+\delta}$ of the Evolved β-$Ni(OH)_2$ Electrode for Selective Oxidation of 5-Hydroxymethylfurfural. *Adv. Mater.* **2023**, *35*, 2211177.

---

(64) Lia, X.; Hoshib, T.; Li, L.; Pu, T.; Zhang, T.; Xie, T.; Li, X.; Ao, J.-P. GaN Schottky Barrier Diode with Thermally Stable Nickel Nitride Electrode Deposited by Reactive Sputtering. *Mater. Sci. Semicond. Process.* **2019**, *93*, 1-5.

(65) Buckley, A. N.; Woods, R. Electrochemical and XPS Studies of the Surface Oxidation of Synthetic Heazlewoodite (Ni_3S_2). *J. Appl. Electrochem.* **1991**, *21*, 575-582.

(66) Legrand, D. L.; Nesbitt, W. H.; Bancroft, G. M. X-Ray Photoelectron Spectroscopic Study of a Pristine Millerite (NiS) Surface and the Effect of Air and Water Oxidation. *Am. Mineral.* **1998**, *83*, 1256–1265.

(67) Murthy, A. P.; Theerthagiri, J.; Madhavan, J. Insights on Tafel Constant in the Analysis of Hydrogen Evolution Reaction. *J. Phys. Chem. C* **2018**, *122*, 23943−23949.

(68) Zheng, Y.; Jiao, Y.; Jaroniec, M.; Qiao, S. Z. Advancing the Electrochemistry of the Hydrogen-Evolution Reaction Through Combining Experiment and Theory. *Angew. Chem. Int. Ed.* **2015**, *54*, 52–65.

(69) You, B.; Liu, X.; Hu, G.; Gul, S.; Yano, J.; Jiang, D.; Sun, Y. Universal Surface Engineering of Transition Metals for Superior Electrocatalytic Hydrogen Evolution in Neutral Water. *J. Am. Chem. Soc*. **2017**, *139*, 12283–12290.

(70) Park, S.; Liu, L.; Demirkır, Ç.; van der Heijden, O.; Lohse, D.; Krug, D.; Koper, M. T. M. Solutal Marangoni Effect Determines Bubble Dynamics during Electrocatalytic Hydrogen Evolution. *Nat. Chem.* **2023**, *15*, 1532–1540.

(71) Bashkatov, A.; Park, S.; Demirkır, Ç.; Wood, J. A.; Koper, M. T. M.; Lohse, D.; Krug, D. Performance Enhancement of Electrocatalytic Hydrogen Evolution through Coalescence-Induced Bubble Dynamics. *J. Am. Chem. Soc.* **2024**, *146*, 10177–10186.